J. Plasma Physics (2013), vol. 79, part 5, pp. 597–612. © Cambridge University Press 2013
doi:10.1017/S0022377813000147

Turbulence evolution in MHD plasmas

MARTINA WISNIEWSKI[1], RALF KISSMANN[2]
and FELIX SPANIER[1]

[1]Lehrstuhl für Astronomie, Universität Würzburg, Emil-Fischer Str. 31, D-97074 Würzburg, Germany
(fspanier@astro.uni-wuerzburg.de)
[2]Institut für Astro- und Teilchenphysik, Universität Innsbruck, Innsbruck, Austria

(Received 25 June 2012; revised 18 December 2012; accepted 15 January 2013; first published online 21 February 2013)

Abstract. Turbulence in the interstellar medium has been an active field of research in the last decade. Numerical simulations are the tool of choice in most cases. However, while there are a number of simulations on the market, some questions have not been answered finally. In this paper, we examine the influence of compressible and incompressible driving on the evolution of turbulent spectra in a number of possible interstellar medium scenarios. We conclude that the driving has an influence not only on the ratio of compressible to incompressible component but also on the anisotropy of turbulence.

1. Introduction

Turbulence in the context of the interstellar medium (ISM) was for the first time discussed by von Weizsäcker (1951). This discussion, however, was soon abandoned by the scientific community. Until the late 1970s, there was not much progress in the field of interstellar turbulence. Only when the observational techniques became better at this time it became clear that there were power-law correlations between different structures in the ISM. As first turbulence was only connected to the smallest scales of the ISM but with improved observations, it was found that turbulence was present at all spatial scales. A corresponding spectrum of the density fluctuations can be found in e.g. Armstrong et al. (1995).

Besides the well-known density fluctuation spectra, velocity power spectra may also be obtained. One possible method for this was presented by Lazarian and Pogosyan (1997) and was applied by Padoan et al. (2006). The connection between the velocity and density observations is not fully understood, as pointed out by Klessen (2000). For the case of the magnetic field, structure functions may be observed with radio telescopes (e.g. Haverkorn et al. 2004). For a more detailed account of the observational evidence for interstellar turbulence, see Elmegreen and Scalo (2004).

Since there are yet no *in situ* measurements of the ISM, a number of questions are still not resolved. One of those is the question of compressibility. Many theories assume an incompressible medium, yet this is not compatible with the density fluctuation observations in the ISM. In the wave picture of interstellar turbulence (Lazar et al. 2003; Spanier and Schlickeiser 2005), it may well be assumed that up to certain wave numbers a major compressible component is present. Another issue which is not yet fully answered is the question of the driving of the turbulence. The energy balance of the ISM suggests that supernovae are the driving force and energy is dissipated at small scales. Whether this driving is compressible or incompressible is not clear. On the one hand, the driving scenario involving supernova shock waves is connected to compression, since the shocks themselves are compressed. On the other hand, streaming cosmic rays may also be a source of driving especially through incompressible Alfvén waves (Skilling 1975).

In the course of this paper, we will recall the main theories for anisotropic magnetohydrodynamic (MHD) turbulence and review recent simulations. We then present the results of our simulations and their implications for the understanding of compressible MHD turbulence.

In this paper, at first we discuss the current knowledge about the theory of plasma turbulence, then we will present our numerical methods. The results are shown for short time scales of turbulent driving, the evolving spectrum during driving and the saturated spectrum.

2. Theory

2.1. Turbulence theory

From the theoretical side, the discussion about a turbulence theory started out from the investigation of incompressible turbulence described by the Navier–Strokes equation. The early discussions by Kolmogorov (see e.g. Kolmogorov 1941) used the assumption of spatially homogeneous turbulence. Later on, however, it was found that intermittency had to be taken into account, leading to a slightly different form of the velocity spectrum. For different intermittency models and a general overview of the turbulence, see Frisch (1995). For the turbulence in a magnetized fluid, the model by She and Leveque (1994) was extended to include compressibility and a magnetic field. Politano and Pouquet (1995) have discussed the

https://doi.org/10.1017/S0022377813000147 Published online by Cambridge University Press

role of intermittency in the solar wind, proposing sheet like structures (also discussed in Grauer et al. 1994).

The next important step is the inclusion of a background magnetic field. In Shebalin et al. (1983), numerical studies have been conducted showing anisotropies of MHD plasmas due to the background field. This aspect was addressed by Sridhar and Goldreich (1994), where the authors use a heuristic wave model to get some idea of the anisotropy of the turbulence spectrum of magnetic turbulence with a background field. The effects of a background magnetic field, however, are by no means fully understood. This is reflected by the debate started in Goldreich and Sridhar (1995), where a discussion about the correct description of parallel and perpendicular cascades started. Another aspect is the question when turbulence can be described by a wave-interaction picture and when non-linear processes dominated instead.

To resolve this question, a number of simulations have been conducted in the last 15 years. The first numerical test was conducted by Cho and Vishniac (2000), a prominent example is the simulations by Maron and Goldreich (2001), who consider simulations of decaying incompressible turbulence. The incompressible plasma attracts far more attention by modellers for a number of reasons. A prominent one is that incompressible plasmas may be simulated with spectral methods providing a spectrum extending to high wave numbers. Apart from that, basic turbulence theories are mainly developed for incompressible fluids. But Chandran (2005) has also done additional work on compressible turbulence in the $\beta \ll 1$ limit for the evolved spectra. Due to the very low β limit, sound waves are neglected in these simulations. Here, however, we will show the importance of sound waves in the context of compressible plasmas. A work which is more closely related to ours is that of Kuznetsov (2001), where the author investigated compressible plasmas with high and low values of β. In his approach, only weak turbulence is considered. As mentioned above, it is not yet clear if a wave picture is applicable, but in the weak turbulence limit the wave picture is explicitly assumed. Additionally, a theoretical description including major cooling and damping mechanisms for the ISM has been presented by Lithwick and Goldreich (2001). Here, different β regimes are discussed.

2.2. Excitation of MHD waves with compressible or incompressible distortions

In Federrath et al. (2008, 2010), a discussion similar to our discussion regarding the influence of compressible versus incompressible driving has been started. However, this discussion was limited to hydrodynamic simulations of the ISM. A more recent paper (Federrath et al. 2011) added the magnetic field and discussed the effect of turbulent magnetic field growth. We will extend this discussion in the case of magnetized fluids to the anisotropies present in the driven turbulence. This discussion has been continued by Lemaster and Stone (2009), who did simulations of MHD plasmas, but limited themselves to incompressible driving but with variations of the peak wave number of the driver. They showed that approximately a factor of 128 between the driving peak and the total resolution is sufficient for convergence.

2.2.1. Compressible driving. We inject compressible disturbances isotropically into our simulation domain. These disturbances can distort the magnetic field and so excite waves. The induction equation shows us which waves can be expected. Without loss of generality, the preferred direction of the magnetic field can be chosen to be the x-direction (defined by the unit vector $\mathbf{e}_x$). For the induction equation, we find that

$$\frac{\partial \mathbf{B}}{\partial t} = -\nabla \times \mathbf{E} = \nabla \times (\delta \mathbf{v} \times B\mathbf{e}_x), \tag{2.1}$$

where we used $\mathbf{E} = -\delta \mathbf{v} \times \mathbf{B}$ for the electric field which holds for ideal plasmas. If the compressible fluctuations are in the x-direction, no magnetic field will be injected as $(\delta v \mathbf{e}_x \times \mathbf{B} \cdot \mathbf{e}_x) = 0$. If the distortion is perpendicular to the background field (e.g. $\delta \mathbf{v} = v\mathbf{e}_y$), this results in a distortion of the magnetic field in the x-direction:

$$\frac{\partial \mathbf{B}}{\partial t} = ik\mathbf{e}_y \times (\delta v \mathbf{e}_y \times B\mathbf{e}_x), \tag{2.2}$$

$$\frac{\partial \mathbf{B}}{\partial t} = ik\mathbf{e}_y \times (-v)B\mathbf{e}_z,$$

$$\frac{\partial \mathbf{B}}{\partial t} = -i\mathbf{e}_x kvB, \tag{2.3}$$

where we used $\nabla = ik\mathbf{e}_y$ as for compressible waves $\mathbf{k}$ is parallel to $\delta \mathbf{v}$

For the case $\delta \mathbf{v} = v\mathbf{e}_z$, we also find a distortion of the magnetic field in the x-direction:

$$\frac{\partial \mathbf{B}}{\partial t} = i\mathbf{e}_x kvB. \tag{2.4}$$

As the distortion of the magnetic field is perpendicular to $\mathbf{k}$, we would expect to find compressible waves that propagate in the perpendicular direction with respect to the mean magnetic field. We can also identify these waves as for MHD waves and the propagation in the perpendicular direction is only possible for fast magnetosonic waves.

2.2.2. Incompressible driving. Here we want to figure out if Alfvén waves being the only incompressible waves in MHD plasmas can be generated from those incompressible fluctuations. As for incompressible fluctuations, $\mathbf{k}$ is parallel to the background field $\nabla = k\mathbf{e}_x$. So, we find for the magnetic field

$$\frac{\partial \mathbf{B}}{\partial t} = k\mathbf{e}_x \times (\delta v \mathbf{e}_y \times B\mathbf{e}_x) = \mathbf{e}_y kvB \tag{2.5}$$

or

$$\frac{\partial \mathbf{B}}{\partial t} = k\mathbf{e}_x \times (\delta v \mathbf{e}_z \times B\mathbf{e}_x) = \mathbf{e}_z kvB. \tag{2.6}$$

As the distortion of the magnetic field is perpendicular to $\mathbf{k}$, this results in Alfvén waves propagating parallel with respect to the mean magnetic field.

https://doi.org/10.1017/S0022377813000147 Published online by Cambridge University Press

2.3. Three-wave interaction

A three-wave interaction is used to describe the interaction of compressible and incompressible waves in a weakly turbulent plasma and has been described in the first place by Chin and Wentzel (1972). Applications to high- and low-β plasmas are discussed in Vainio and Spanier (2005).

For our investigations, where we drive with either pure compressible or pure incompressible fluctuations, one has to put the question with which process compressible fluctuations are generated from incompressible fluctuations and the other way around. As this happens for small turbulent amplitudes, we claim that three-wave interactions are the key process.

Here a validation is carried out how Alfvén waves are generated by fast magnetosonic waves. It is also shown what can be predicted about the propagation direction of the resulting Alfvén waves. The calculation of the generation of fast magnetosonic waves from Alfvén waves can be done analogously.

In principle, Alfvén waves can be generated from fast magnetosonic waves by either of two processes:

$$A^+ + F^- \leftarrow A^\pm, \tag{2.7}$$

$$A^+ + A^- \rightarrow F^\pm. \tag{2.8}$$

Here, we will restrict the discussion to the special case of perpendicular propagating fast magnetosonic waves with $\beta \ll 1$. For this, we find the phase velocity of these waves to be

$$v_{ph} \approx (\sqrt{1+\beta}) v_A. \tag{2.9}$$

In this case, the reaction equation (2.9) provides no valid solution when computing the resonance condition (i.e. the energy equation). For reaction equation (2.8), however, we find the following resonance condition:

$$v_A(k^+_{A,\|} + k^-_{A,\|}) = v_A(\sqrt{1+\beta}) k^\pm_F, \tag{2.10}$$

$$v_A(k^+_{A,\|} + k^-_{A,\|}) = v_A(\sqrt{1+\beta})((k^+_{A,\|} - k^-_{A,\|})^2 + k^\pm_{F,\perp})^{1/2} \tag{2.11}$$

with

$$k^+_{A,\|} - k^-_{A,\|} = \pm k^\mp_{F,\|} k^+_{A,\perp} + k^-_{A,\perp} = \pm k^\mp_{F,\perp}. \tag{2.12}$$

As the fast magnetosonic waves propagate in the perpendicular direction $k_{F,\|} = 0$ and so with (2.11) and (2.12), we find for the parallel component of the fast magnetosonic waves:

$$k^+_{A,\|} = k^-_{A,\|} = \frac{1}{2} k_{F,\|} \sqrt{1+\beta}. \tag{2.13}$$

For the perpendicular component of the fast magnetosonic waves, we find

$$\langle k^\pm_{A,\perp} \rangle = \frac{1}{2} k_{F.} \tag{2.14}$$

With that we find that

$$\tan\theta = \frac{k_{A,\|}}{k_{A,\perp}} = \frac{\frac{1}{2} k_F \sqrt{1+\beta}}{\frac{1}{2} k_F} = \sqrt{1+\beta}, \tag{2.15}$$

where θ is the angle between the propagation direction of the fast magnetosonic waves and the Alfvén waves. As $\beta \ll 1$, it can be followed that $\tan\theta \approx 1$. This gives us a preferred propagation direction for the Alfvén waves close to $\theta = 45^\circ$.

A similar study has been undertaken by Chandran (2008) for the low-β case taking into account also fast magnetosonic wave. Lithwick and Goldreich (2001) have discussed systems with high and low β, and their approach is an analytical one.

3. Numerical simulations

3.1. MHD equations

For our studies, we used the ideal MHD equations in a periodic domain, where the system is closed by an isothermal equation of state. Since our analysis is a principal one, we will give all variables in non-dimensional, normalized units. For that purpose, all variables are split into a dimensionless variable of order unity and a normalization constant. Here, we use four independent variables for the normalization: the length of the simulation domain L, the mass of the hydrogen atom m_0, a typical number density n_0, and the temperature of the system T_0 which directly relates to the speed of sound c_s. Therefore, length scales are normalized as $x = L\tilde{x}$, velocity as $u = u_0\tilde{u} = c_s\tilde{u}$, density as $\rho = m_0 n_0 \tilde{\rho}$ and so forth. The resulting set of normalized MHD equations is the following:

$$\frac{\partial \rho}{\partial t} = -\nabla \mathbf{s}, \tag{3.1}$$

$$\frac{\partial \mathbf{s}}{\partial t} = -\nabla \left(\frac{\mathbf{ss}}{\rho} + \left(p + \frac{B^2}{2} \right) 1 - \mathbf{BB} \right) + \mathbf{F}, \tag{3.2}$$

$$\frac{\partial \mathbf{B}}{\partial t} = -\nabla \left(\frac{\mathbf{sB} - \mathbf{Bs}}{\rho} \right), \tag{3.3}$$

$$p = \frac{c_s^2}{u_0^2} \rho \overset{\text{(here)}}{=} \rho. \tag{3.4}$$

Here, ρ is the mass density, $\mathbf{s} = \rho\mathbf{v}$ is the momentum density and $\mathbf{B}$ indicates the magnetic induction and p is the thermal pressure. The isothermal equation of state (3.4) is simplified due to our choice for the normalization constants.

In the following, we will classify our results on the basis of β we used for our simulations. We only use it for the initialization of the unperturbed background magnetic fields. It is defined as the fraction of the thermal and magnetic pressure.

3.2. Numerical model

For the time evolution of the MHD equations, we use a second-order centrally weighted essentially non-oscillatory (CWENO) algorithm (see e.g. Kurganov and Levy 2000). It is very convenient for the simulation of shocks as we find them in fluids and plasmas. In

https://doi.org/10.1017/S0022377813000147 Published online by Cambridge University Press

the mathematical description, these shocks are so-called 'Riemann problems' and their accurate numerical treatment with a Godunov solver results in high numerical costs. The CWENO scheme avoids to solve these Riemann problems directly by averaging over the appropriate fractions of every cell. Additionally, oscillations are suppressed by the reconstruction. This results in a fast scheme for the treatment of the MHD equations with passable small dissipation. This CWENO method is combined with a third-order Runge–Kutta algorithm which has been chosen because of the small memory costs with comparatively high resolution in time, due to the fact that only one additional field has to be buffered.

Besides the direct numerical simulation technique large eddy simulation has been used. This is for example demonstrated in Chernyshov et al. (2007, 2009) for the case of decaying turbulence. We are refraining from using this method since it requires a number of implications on the turbulent cascade on small scales which we are not sure of.

3.3. Turbulence driver

For the external stirring of the fluctuations, we define a function f in Fourier space with

$$f_k = sk^{-7/4}\exp(2\pi\imath p), \tag{3.5}$$

where 's' and 'p' are random numbers between zero and one. The random number generator for the former of these obeys a Gaussian distribution, whereas the latter is uniformly distributed. This function f_k yields the Fourier space distribution of the velocity fields used for driving the fluctuations in our simulations. After transforming to configuration space $f_k \longrightarrow f_x$, we make the distinction between the cases of compressible and incompressible driving. For the former, we use $\delta\mathbf{v} = \nabla f_x$, whereas for the latter we employ $\delta\mathbf{v} = \nabla \times \mathbf{f}$. As $\mathbf{f}$ has, thus, to be a vectorial function in the case of incompressible driving, we define each component separately with different random numbers. Each component of the wave vector $\mathbf{k}$ in our Fourier space spectra ranges from one to eight, yielding a maximum absolute value of $|\ \mathbf{k}\ | \leqslant 13$. The perturbations are set up in a form such that no net momentum is added to the numerical domain. The energy input is normalized to an estimate for the average energy input by supernovae into the ISM of our Galaxy into a volume of the size of the simulation domain. The resulting driving spectrum is isotropic and it yields $v^2(k) \propto k^{-3/2}$, which yields a production spectrum harder than the anticipated inertial spectrum.

Finally, we define the compressible and incompressible energy spectra. Both are calculated in Fourier space on the basis of the velocity fields with

$$P_{\mathrm{comp}}(k) \equiv \frac{1}{2}\left\|\widehat{k}\cdot\mathbf{v}(\mathbf{k})\right\|^2, \tag{3.6}$$

$$P_{\mathrm{incomp}}(k) \equiv \frac{1}{2}\left\|\widehat{k}\times\mathbf{v}(\mathbf{k})\right\|^2, \tag{3.7}$$

where $\widehat{k}$ is the normalized wave vector. The overall energy spectrum of the velocity fields is

$$P_K(k) \equiv \frac{1}{2}v^2(k), \tag{3.8}$$

where the sum of $P_{\mathrm{comp}}(k)$ and $P_{\mathrm{incomp}}(k)$ is $P_K(k)$. In the following discussion, we have to make an important differentiation: P_K is the power spectrum of velocity fields in the whole system, whereas P_K^* is the power spectrum of the velocity fields of the driver. This is important because the turbulent energy of the velocity fields of the whole system does not have to accord to the driving spectrum. This will be important in Sec. 4.1.2. Additionally, we define the omnidirectional energy spectrum of the magnetic fields with

$$P_B \equiv \frac{1}{2\bar{\rho}}\delta B^2(k). \tag{3.9}$$

3.4. Simulation set-up

For all our investigations, we use in principle the same simulation set-up. We start out from an unperturbed plasma with a homogeneous background magnetic field and inject with each time step either compressible or incompressible energy with our turbulence driver explained in Sec. 3.3. We do this for compressible and also for incompressible driving and both runs are performed for $\beta = 0.01$ and $\beta = 10$. This enables us to analyse the influence of the different drivings on as well the highly magnetized as the quite hydrodynamic plasmas. So the basis of the following research is those four runs. With the simulation output we gain during the simulation, we calculate the turbulent energy spectra defined in Sec. 3.3.

4. Results

Here, we will discuss three distinct topics relating to our simulation results. First, we investigate the physics on short and intermediate timescales where the fluctuations of the velocity fields excite modes. This is done in Sec. 4.1. Then the time evolution of the energies is studied in Sec. 4.2. Finally, an investigation of the convergence range is done in Sec. 4.3. In order to quantify the anisotropy, we use a scalar parameter which is derived from two-dimensional spectra. The parameter is described in detail in the Appendix.

4.1. Short time scales

This investigation is of special interest because it can be observed how the first waves are generated for compressible as well as for incompressible driving and how these waves interact with each other. On the basis of this research, we can determine which processes dominate the turbulence for small amplitudes of the fluctuations. When taking the supernova injection scenario for granted, the build-up of turbulence is a transient phenomenon which may even be observed close in time and space to the energy source. One observable could be

https://doi.org/10.1017/S0022377813000147 Published online by Cambridge University Press

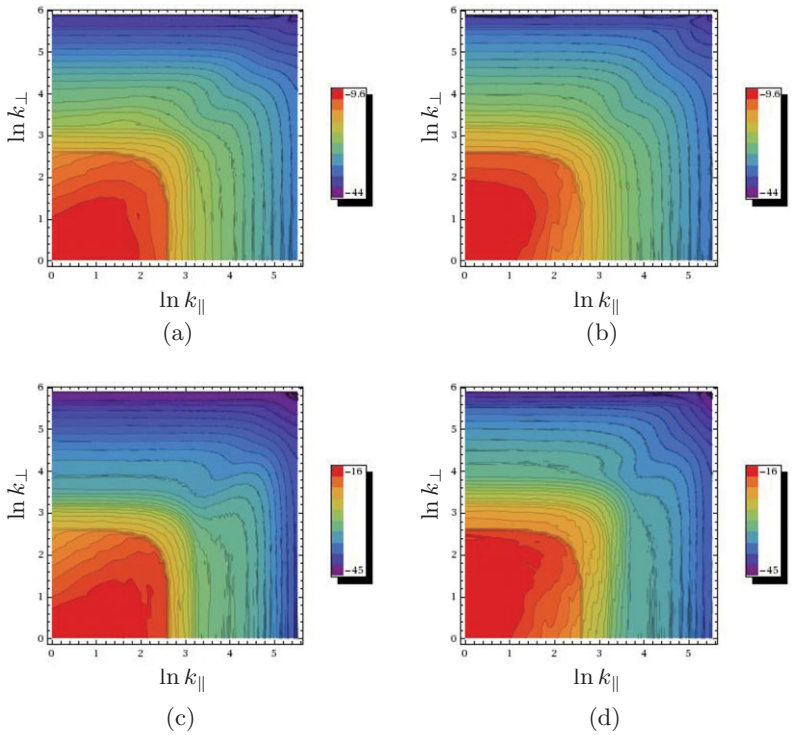


Figure 1. (Colour online) Turbulence spectra P_B after $t = 5 \times 10^{-3}$ simulated on a 512^3 grid. The colour denotes the natural logarithm of the numerical energy. (a, c) $\beta = 10$ incompressible driving; (b, d) $\beta = 10$ compressible driving.

accelerated particles in the upstream of supernova and their respective electromagnetic emission.

For the investigation of the two-dimensional spectra, we need to keep in mind that after this short amount of time we have to distinguish between the driving region that is dominated by the driving spectrum injected for each time step and the part of the spectrum that can only be reached via a cascade. After this short amount of time, the cascading process has only taken place to some extent, so we concentrate mostly on the driving region. Via the intersection points of the contour lines with the $k_\perp$- and $k_\parallel$-axes, we can access the anisotropy of the turbulent fields.

4.1.1. P_B. Figures 1(a)–(d) show the two-dimensional spectra of P_B. We see for both drivings and values of the plasma-β a very anisotropic spectrum ($k_\perp^{\mathrm{aniso}}(1) = 2$) within the driving range. The spectra show a remarkable feature. For incompressible driving, contour lines in the driving range rise from the $k_\perp$ axis (following the diagonal), while for compressible driving the contour lines rise from the $k_\parallel$ axis. The slope of the contour lines indicates a spectrum which has in parts a positive exponent with respect to k.

There is an explanation for this behaviour, which may be deduced from the fact that the difference exists between compressible and incompressible fluctuations. For the case of incompressible fluctuations, the vector $\delta\mathbf{v}$ is perpendicular to the wave vector $\mathbf{k}$, while for compressible fluctuations, the both vectors are aligned. If we examine now the induction equation for incompressible fluctuations (2.5) moving in parallel direction, we find

$$\frac{\partial \mathbf{B}}{\partial t} = \nabla \times (\delta v \mathbf{e}_y \times B_0 \mathbf{e}_x). \tag{4.1}$$

This yields for the turbulent velocity spectrum

$$\frac{\partial \mathbf{B}}{\partial t} = k_\parallel k^{-3/4} B_0. \tag{4.2}$$

This yields a rising spectrum in parallel spectrum as seen above. It also explains the crossing of the contour line and the $k_\perp$ axis. For the compressible driving the explanation follows the same line, but is essentially different, since the vector $\delta\mathbf{v}$ has a different orientation.

We can make further distinction between $\beta = 0.01$ and 10. If we examine the two-dimensional spectra closely, we find a cut-off in some of the spectra, which may be identified by very close contour lines (as for example in Fig. 1a). For compressible driving, we find a strong cut-off for $\beta = 10$, while it seems to have dissolved already for $\beta = 0.01$. Since the induction equation makes no distinction between the two values of β, it seems that another physical process is taking place here. By examining P_{Comp} and P_{Shear}, we will show later that this may be caused by a mixture of Alfvén and fast magnetosonic waves.

In Figs. 2(a)–(d), the magnetic field after a normalized time of 5×10^{-3} can be seen. One may now compare the eddy size and spectrum (as done for example in Beresnyak and Lazarian 2009) to see at least qualitatively that the elongation of the eddies is correlated with the cut-off seen in the two-dimensional spectra. This is of course not unexpected.

https://doi.org/10.1017/S0022377813000147 Published online by Cambridge University Press

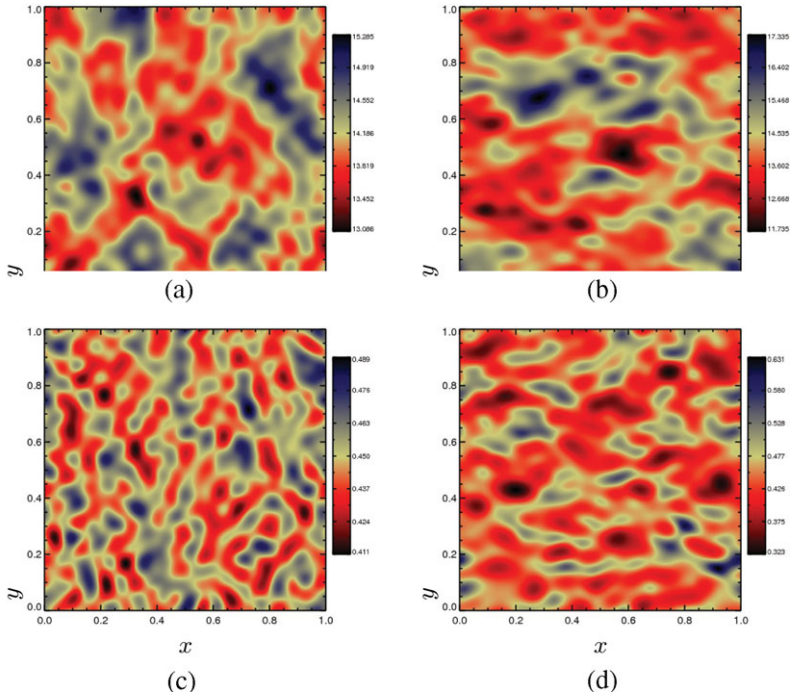


Figure 2. (Colour online) Turbulent magnetic fields after $t = 5 \times 10^{-3}$ in real space on a 512^3 grid. $\beta = 0.01$ incompressible (a) and compressible (b) driving; $\beta = 10$ incompressible (c) and compressible (d) driving.

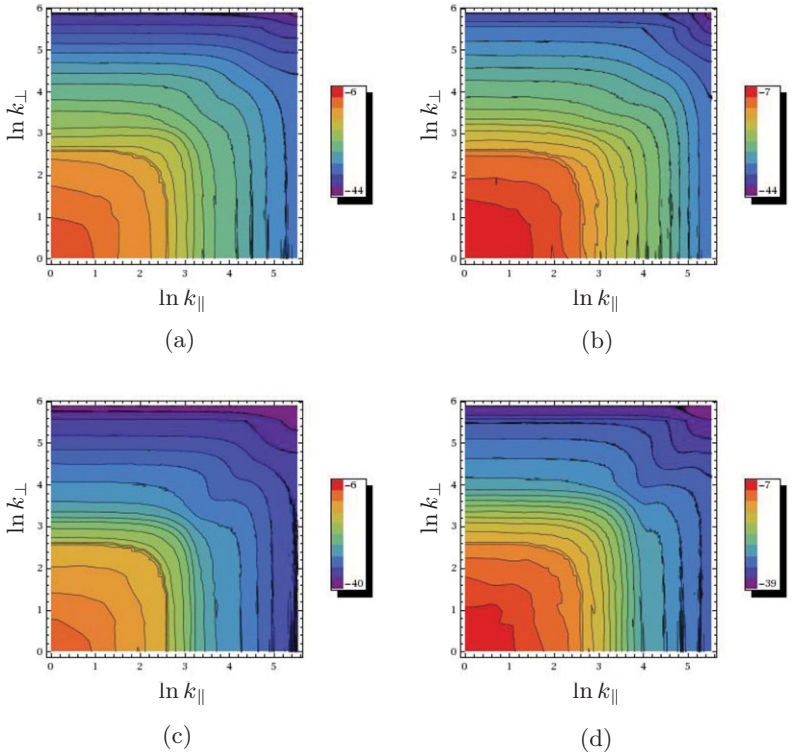


Figure 3. (Colour online) Turbulence spectra P_K after $t = 5 \times 10^3$ simulated on a 512^3 grid. $\beta = 0.01$ incompressible (a) and compressible (b) driving; $\beta = 10$ incompressible (c) and compressible (d) driving.

4.1.2. P_K. Figures 3(a)–(d) show the two-dimensional spectra of P_K for $\beta = 0.01$ and 10 for both compressible and incompressible driving.

For $\beta = 0.01$ and incompressible driving, we see in the driving region of P_K a perpendicular preferred direction ($k_\perp^{\mathrm{aniso}}(1.5) = 1.8$) whereas for $\beta = 0.01$ and compressible driving, we find a parallel preferred direction ($k_\perp^{\mathrm{aniso}}(1.5) = 1.5$) although P_K^* is for both cases isotropic. The term 'preferred direction' is used here when the two-dimensional spectra are anisotropic. The contour lines of

https://doi.org/10.1017/S0022377813000147 Published online by Cambridge University Press

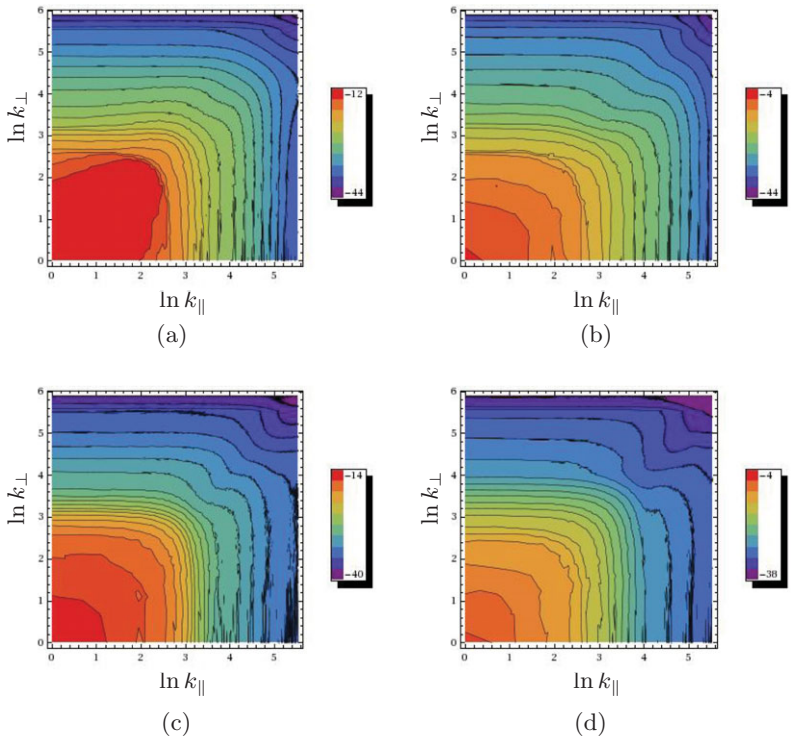


Figure 4. (Colour online) P_{Comp} after $t = 5 \times 10^{-3}$ simulated on a 512^3 grid. $\beta = 0.01$ incompressible (a) and compressible (b) driving; $\beta = 10$ incompressible (c) and compressible (d) driving.

a spectrum with a parallel preferred direction cross the axes for higher values of $k_\parallel$ than $k_\perp$. For the contour lines of a spectrum with a perpendicular preferred direction it is the other way around. For $\beta = 10$, we see for compressible as well as for incompressible driving a very homogeneous driving spectrum. This can be understood quite easily. We drive the turbulence with compressible or incompressible fluctuations in the velocity fields. As shown in Sec. 4.1.1, this results in an excitation of MHD waves in the driving range, so turbulent energy of the velocity fields is transferred into magnetic energy. In the direction of preferred excitation of waves, this energy is missing in the velocity fields and so in P_K. This is why for the case of incompressible driving and $\beta = 0.01$, we find Alfvén waves propagating parallel to the mean magnetic field and so a perpendicular preferred direction in P_K. For compressible driving, we excite fast magnetosonic waves perpendicular to the mean magnetic field which results in a parallel preferred direction of P_K.

For $\beta = 10$, although the same is in all likelihood happening this effect cannot be seen, because the magnetic fields are much weaker and so fewer waves are excited and through this less energy of P_K is transformed into P_B. Hereby, the missing energy in P_K in one of the preferred directions cannot be detected in P_K.

4.1.3. P_{Shear} and P_{Comp}. Now, we will investigate the two-dimensional spectra of P_{Comp} and P_{Shear}. Figures 4(a)–5(d) show the two-dimensional spectra of P_{Comp} and P_{Shear} at a normalized time of 5×10^{-3}. At this very early time, the type of driving dominates the turbulent energy of the velocity fields. Therefore, for $\beta = 0.01$, the driving component shows of course the same behaviour as P_K for $\beta = 0.01$. We also find for compressible driving a parallel preferred direction in P_{Comp} ($k_\perp^{\mathrm{aniso}}(2.2) = 2.0$) as in this case fast magnetosonic waves are generated propagation perpendicular to the mean magnetic field and this energy comes from the turbulent energy of the velocity components. For P_{Shear} and incompressible driving, we find a perpendicular preferred direction ($k_\perp^{\mathrm{aniso}}(1.4) = 1.8$), as we have an excitation of parallel propagating Alfvén waves. The non-driven components – P_{Comp} for incompressible driving and P_{Shear} for compressible driving – show in principle the same diagonal symmetry. In Sec. 2.3, it was shown that Alvén waves can be generated via three-wave interaction from fast magnetosonic waves propagating perpendicular to the mean magnetic field and that these Alvén waves propagate with an angle of 45° to the fast magnetosonic waves. This prediction corresponds to the two-dimensional spectrum of P_{Shear} for compressible driving. The same can be done for P_{Comp} and incompressible driving.

For $\beta = 10$, we find the same P_{Comp} and P_{Shear} limitations as for P_K. Because of the weak magnetic fields only few waves are generated, and this effect becomes as little noticeable as in the driven component as in P_K. As the non-driven component is also absolutely isotropic, no clear conclusion about the dominating physical process can be made.

One should note that there should exist a connection between the P_{comp} results and the density fluctuations through the continuity equation. Density fluctuations

https://doi.org/10.1017/S0022377813000147 Published online by Cambridge University Press

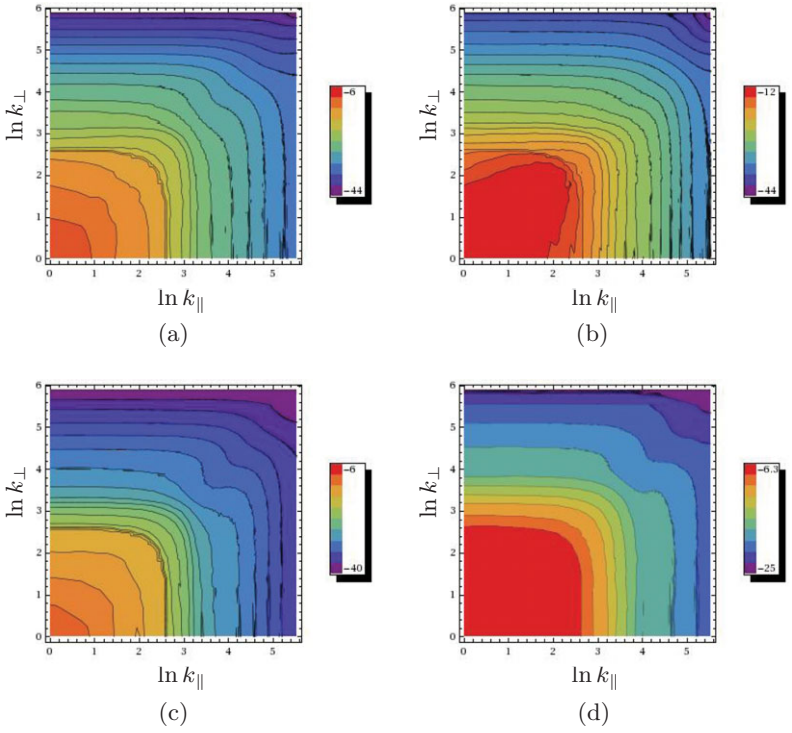


Figure 5. (Colour online) P_{Shear} after $t = 5 \times 10^{-3}$ simulated on a 512^3 grid. $\beta = 0.01$ incompressible (a) and compressible (b) driving; $\beta = 10$ incompressible (c) and compressible (d) driving.

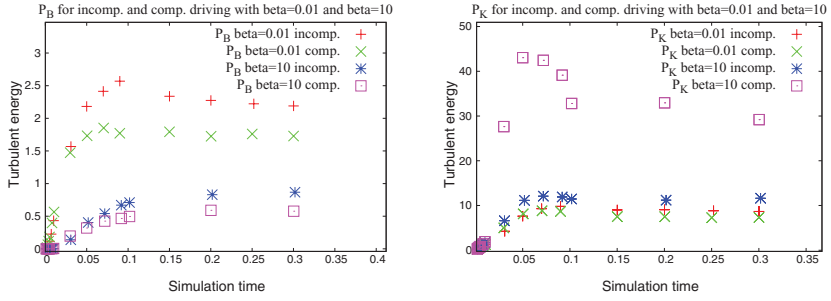


Figure 6. (Colour online) Turbulence spectra P_K and P_B as a function of the simulation time. (a) Turbulent magnetic energy; (b) turbulent energy of the velocity fields.

have been studied in detail by Kowal et al. (2007), where only solenoidal driving is used.

4.2. *Evolving spectrum*

In the following section, P_K, P_{Comp}, P_{Shear} and P_B for the four different set-ups are plotted against the normalized time (see Figs. 6a and b as well as Figs. 8a and b). It can be seen that there is no turbulent energy in the fields at the beginning of the simulation. As the turbulence is driven continuously through the whole simulation, more and more turbulent kinetic energy is injected in the fields with time until the turbulence saturates (this is when the input energy from the driving is balanced by the numerical dissipation). A detailed analysis of the saturation range is given in Sec. 4.3. Here, we are mainly concerned about the physics before convergence is reached. The absolute amplitude of the energies in the convergence range is influenced by numerical effects and so is neglected in the discussion.

4.2.1. Turbulent kinetic energy P_K. The temporal evolution of P_K differs fundamentally between compressible and incompressible driving (see Fig. 6b). This is especially apparent for $\beta = 10$. For compressible driving, we find a distinct maximum for P_K at $t \simeq 0.05$. After that the energy decreases before saturation is reached finally.

What causes the formation of this maximum? In principle, we find for both – compressible and incompressible fluctuations – the same behaviour. If the magnetic field lines are bent, the cascade and so the dissipation of the energy in the system is more efficient. From the data, we can see that for compressible driving, perpendicular fluctuations are generated that decay into the parallel direction, which leads to an isotropic spectrum. To do this, they need a component parallel to the background

https://doi.org/10.1017/S0022377813000147 Published online by Cambridge University Press

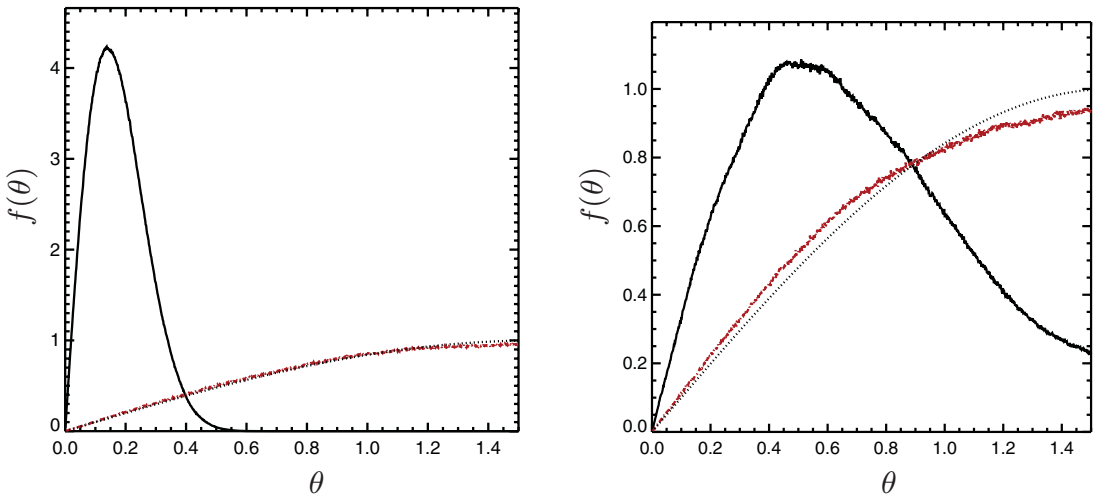
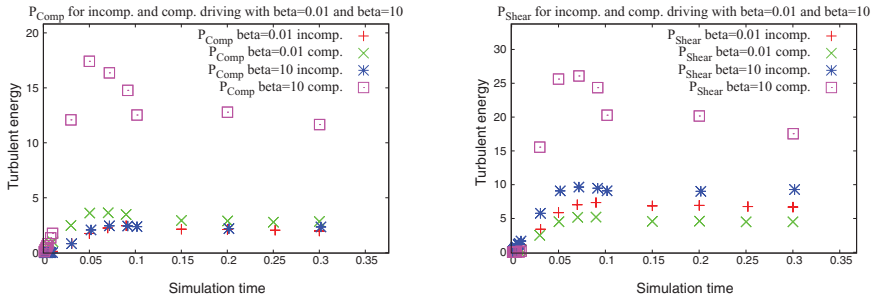
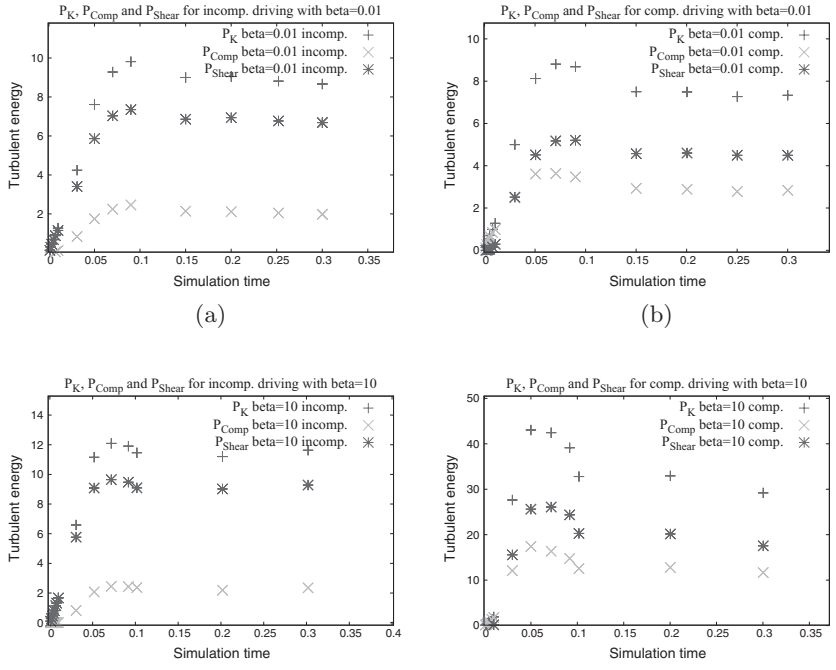


Figure 7. (Colour online) Distribution function of the magnetic field angle for different times and different numerical simulation runs – all results are shown for $\beta = 10$. On the left, we show results for the incompressibly driven turbulence for $t = 0.01$ (black curve) and for $t = 0.3$ (red curve). On the right, the results for compressible (black curve) and incompressible driving (red curve) are compared for $t = 0.05$. In both plots, the dashed line indicates homogeneous distribution.



(a) (b)

Figure 8. (Colour online) Turbulence spectra P_{Comp} and P_{Shear} as a function of the simulation time. (a) $\beta = 0.03$ incompressible driving; (b) $\beta = 10$ incompressible driving.



(a) (b)

(c) (d)

Figure 9. (Colour online) Total turbulent energies P_K,P_{Comp} and P_{Shear} as a function of the simulation time. (a, b) $\beta = 0.01$ incompressible (a) and compressible (b) driving; (c,d) $\beta = 10$ incompressible (c) and compressible (d) driving.

https://doi.org/10.1017/S0022377813000147 Published online by Cambridge University Press

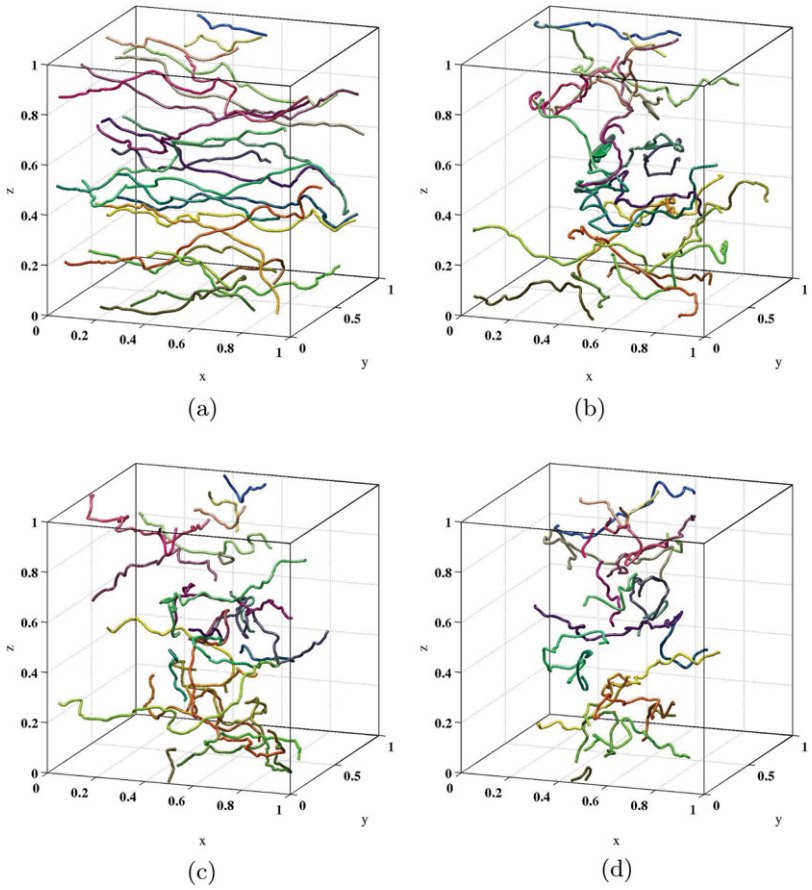


Figure 10. (Colour online) Magnetic field lines for $\beta = 10$ with compressible and incompressible driving. Magnetic field lines for $\beta = 10$ with compressible driving after $t = 0.05$ (a) and $t = 0.3$ (b); magnetic field lines for $\beta = 10$ with incompressible driving after $t = 0.05$ (c) and $t = 0.3$ (d).

magnetic field. If the background field is quite tangled, the fluctuations have a parallel component locally and can decay. For incompressible driving, parallel fluctuations are generated that decay into perpendicular direction and so they need a perpendicular component to the background field. This is why they as well can only decay in a tangled field. The formation of the maximum can occur if the driving energy will bend the magnetic field lines only insufficiently. So, for quite a long time, there would not be a cascade and the resulting dissipation of the energy. Hereby, a larger amount of energy is accumulated until the field lines are bent enough to build up the cascade. Then, the accumulated energy for small $\mathbf{k}$ can at last be reduced by the cascade and the combined dissipation. If the driving energy bends the magnetic field lines efficiently from the beginning, the cascade will build up from the beginning. Through this no energy is accumulated and no maximum will occur. The magnetic field lines for compressible and incompressible driving at this maximum ($t = 0.05$) and after convergence is reached are shown in Figs. 10(a)–(d). It can be seen that for the case of compressible driving, the magnetic field lines are still quite smooth at the maximum whereas in the convergence range they are quite tangled. For the case of incompressible driving, however, the field lines are already quite tangled at $t = 0.05$. This can be understood when considering how the driving acts on the fluid. For incompressible driving, we are basically adding eddy-like motions to our fluid. This means that we get some shear flows, which will certainly bend the background field lines. When adding a compressible velocity field, however, the background field even remains undisturbed for some of the input wave modes. This shows that an incompressible driving field will tangle the field lines much more efficiently. Thus, we find for $\beta = 10$ that with the incompressible driving field the field is tangled so early that such an energy storage, as in the case of the compressible driving, cannot form at all.

This tangling of the magnetic field lines can also be accessed quantitatively. For this, we computed the spatial averages of the quantity

$$a = 1 - 2\mu^2, \tag{4.3}$$

where μ is the angle between the local and the initial magnetic field. For this parameter, we find alignment along the initial magnetic field direction for $a = -1$, where a magnetic field that is perpendicular to the initial one would yield $a = 1$. Due to the fact that there is a higher degree of freedom for the perpendicular direction, an isotropic distribution would yield $a = 1/3$. With this in mind, we can discuss the results for our simulations.

https://doi.org/10.1017/S0022377813000147 Published online by Cambridge University Press

For an initial plasma-β of $\beta = 0.01$, the alignment parameter a even for the saturated turbulence at $t = 0.3$ never exceeds values of -0.9, which is still very parallel. For $\beta = 10$, however, the situation is very different. In this case, we find at $t = 0.05$ (which is the time, when the peak in the energy evolution is most prominent), on the one hand, a nearly isotropic distribution with $a = 0.296$ for the incompressible driver. For compressible driving, on the other hand, we find $a = -0.158576$, where both of these simulations show isotropic distributions at $t = 0.3$. This shows that the compressibly driven simulations with $\beta = 10$ are the only ones for which the tangling of the field lines still changes significantly between $t = 0.05$ and the saturated state. This is also illustrated by the distribution functions shown in Fig. 7 for some of the simulations with $\beta = 10$. In the left panel, we show the distribution function for very early times, where the magnetic field is still pretty much aligned, and the distribution for the saturated state, which is obviously quite isotropic (here one has to take into account that an isotropic distribution in all spatial directions yields a distribution of the form $\sin\theta$ when projected from 3D to a $B_\parallel - B_\perp$ distribution function). In the right panel, we compare the situation for incompressible and compressible driving at the time of the maximum. Apparently, the distribution is still much more aligned for the compressibly driven simulation.

In this context, the simulations of Beresnyak and Lazarian (2009) should be mentioned. Taking into account a partially similar situation, they also evaluate multi-dimensional spectra, but follow a different approach. While in this paper the global frame of reference is used (the axes are determined by the background magnetic field), they are using a local frame of reference. The discussion on which of these two approaches is the best is tedious and maybe not helpful. Looking at Fig. 7, we see that there is a clear bending of field lines, which would suggest using the local frame. But in our opinion there are two major drawbacks using the local frame: (i) the definition of the local frame is not completely unique and may be governed by cut-off effects, (ii) in the case of very weak turbulence, the local and global frame will be equivalent, while for very strong turbulence we may see differences in the local frame picture, which will, in the end, not affect the global picture (which is usually the one being observed).

4.2.2. P_B. For early times, it can be seen that P_B has higher values for compressible than for incompressible driving (see Fig. 6a and Table 1). This is due to the fact that for incompressible driving, Alfvén waves are generated propagating in the x-direction, whereas for compressible driving fast magnetosonic waves are generated propagating within the whole perpendicular y–z plane. Therefore, the magnetosonic waves have an additional degree of freedom for their excitation and because of that more fast magnetosonic waves than Alfvén waves are excited for the same driving strength and driving time. During the whole simulation, much more turbulent energy of the velocity fields is converted into magnetic energy for small β than for high β. This is due to the fact that the background magnetic field is stronger for small plasma-βs, which yields stronger magnetic fluctuations by tangling the velocity fields.

In addition, P_B sometimes shows a maximum before it reaches the saturation range (e.g. for $\beta = 0.01$ and incompressible driving at 0.09 in Fig. 6a). But in this case, it barely depends on the driving but on β. This is because the rate at which magnetic energy is converted from the velocity fields depends strongly on β. For $\beta = 10$, this rate is anyway so small that even a quite inefficient cascade is adequate to remove enough energy that no maximum can build up. For small β, the energy is converted fast enough that, in principle, a maximum can build up. As for the case of incompressible driving, more energy is converted in the saturation range and the maximum is even slightly higher (see Fig. 6a for $\beta = 0.01$ and incompressible driving at 0.09 as well as for $\beta = 0.01$ and compressible driving at 0.075).

4.2.3. P_{Shear} and P_{Comp}. P_{Shear} and P_{Comp} are plotted in Figs. 8(a)–(b) and 9(a)–(d) together with the total energy of the velocity fields P_K. In Table 2, the energies are listed for a normalized time of 5×10^{-3} and for the saturated state of the spectrum.

At the beginning of the simulation, the energy of the driving component is higher for $\beta = 10$ than for $\beta = 0.01$. This is because for bigger plasma-βs, there are

Table 1. Magnetization of the system.

	Driving	β	PB	PK	$\frac{PB}{PK}$
Time 0.05	Incomp.	0.01	9.2769×10^{-3}	0.6986	0.0133
Time 0.05	Comp.	0.01	0.014504	0.70617	0.0205
Time 0.05	Incomp.	10	1.9613×10^{-5}	0.81475	2.407×10^{-5}
Time 0.05	Comp.	10	5.042×10^{-5}	0.828	6.089×10^{-5}
Saturation	Incomp.	0.01	0.177	8.84	0.02
Saturation	Comp.	0.01	0.1383	7.363	0.0188
Saturation	Incomp.	10	0.0675	11.42	5.913×10^{-3}
Saturation	Comp.	10	0.0465	31.05	1.502×10^{-3}

Table 2. Compressible and incompressible energy of the system.

	Driving	β	PShear	PComp	$\frac{P\mathrm{Comp}}{P\mathrm{Shear}}$
Time 0.05	Incomp.	0.01	0.676	0.022	3.25×10^{-2}
Time 0.05	Comp.	0.01	0.0521	0.654	12.55
Time 0.05	Incomp.	10	0.814	3.19×10^{-4}	3.92×10^{-4}
Time 0.05	Comp.	10	6.47×10^{-3}	0.822	127.0
Saturation	Incomp.	0.01	6.80	2.03	0.30
Saturation	Comp.	0.01	4.53	2.82	0.62
Saturation	Incomp.	10	9.14	2.27	0.25
Saturation	Comp.	10	18.86	12.2	0.65

https://doi.org/10.1017/S0022377813000147 Published online by Cambridge University Press

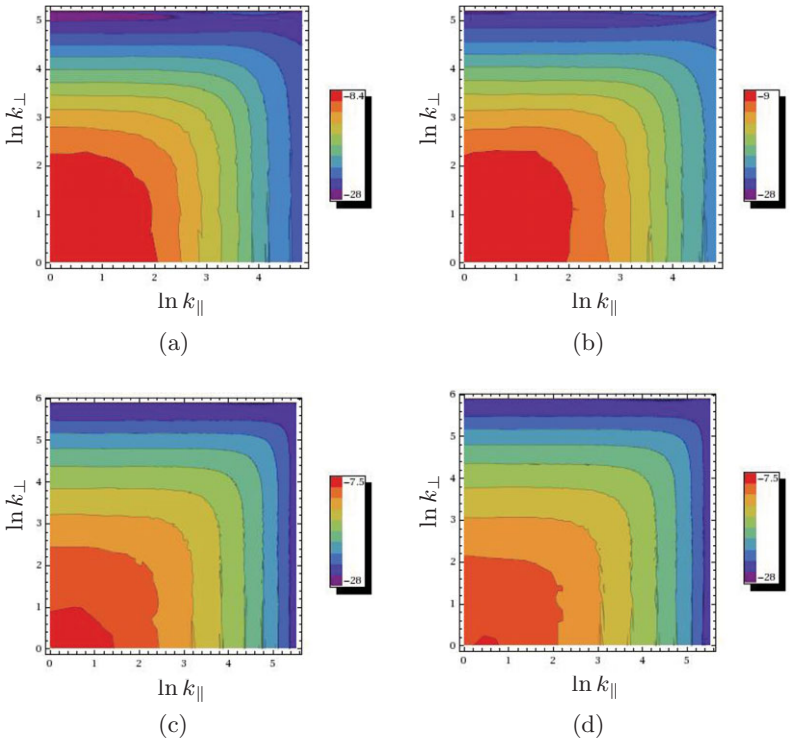


Figure 11. (Colour online) P_B in the saturated state of the turbulence simulated on a 256^3 and a 512^3 grid. $\beta = 0.01$ incompressible (a) and compressible (b) driving simulated on a 256^3 grid; $\beta = 10$ incompressible (c) and compressible (d) driving simulated on a 512^3 grid.

smaller magnetic fields and consequently fewer waves are generated. Therefore, less energy of the driving component is transformed into magnetic energy and hence missing in the energy of the driving component. Additionally, as there are fewer excited modes for $\beta = 10$, the non-driven component is smaller because fewer modes are generated that can decay into other waves and so transform compressible modes into incompressible modes and the other way around. Although the driving dominates P_K in the beginning, it stands out that the incompressible energy after some time dominates P_K, independent of the kind of driving and the plasma-β. The dominance of the incompressible energy might be caused by a more efficient conversion of compressible modes into incompressible modes than the other way around. The saturated results given in Sec. 4.3 support this idea.

4.3. Saturated state of the spectrum

The saturated state of the spectrum has been described in a number of previous papers (e.g. Cho and Lazarian 2002, 2003). While Cho and Lazarian (2002) concentrated on the simulation of low-β plasmas, Cho and Lazarian (2003) also considered high-β plasmas. In both cases, incompressible driving was used. As discussed above, we will also use compressible driving, which may be motivated by supernova shock waves driving the ISM. Another point which is different is that the authors of the aforementioned studies attempted the decomposition into different wave modes. Our approach will focus on the decomposition in irrotational and solenoidal fields. This is specifically useful when one assumes that the turbulence is dominated by shocks.

Here, we present the two-dimensional spectra for the saturated state of the turbulence. For $\beta = 0.01$ and compressible driving P_K, P_{Shear} and P_{Comp} have a clearly parallel preferred direction (see Figs. 12b, 13b and 14b). In the saturated state, we are concerned with fully nonlinear interactions, which form an anisotropic cascade, as we see from the results. For incompressible driving, we find that P_K and P_{Shear} develop a perpendicular preferred direction (see Figs. 12a and 13a), as has been predicted by Shebalin et al. (1983). The spectrum of P_{Comp}, however, is quite isotropic (see Fig. 14a). As already mentioned in Sec. 4.2.3, we believe that compressible modes may easily be converted into incompressible modes, but not the other way around. This is confirmed by the two-dimensional spectra, because for compressible driving P_{Shear} has the same anisotropy as P_{Comp}. Actually, the incompressible modes would build up a perpendicular cascade, as can be seen by the results in Figs. 12(a) and 13(a); as they are however directly generated by the compressible modes, the cascade is forced to build up the same preferred direction. Contrariwise, in the case of incompressible driving, P_{Comp} has not the same preferred direction as P_{Shear}. So, the transformation of compressible modes from incompressible modes is not that efficient. This is why a superposition of compressible and incompressible modes and so of a parallel and perpendicular cascade can be seen. The result is an isotropic spectrum.

https://doi.org/10.1017/S0022377813000147 Published online by Cambridge University Press

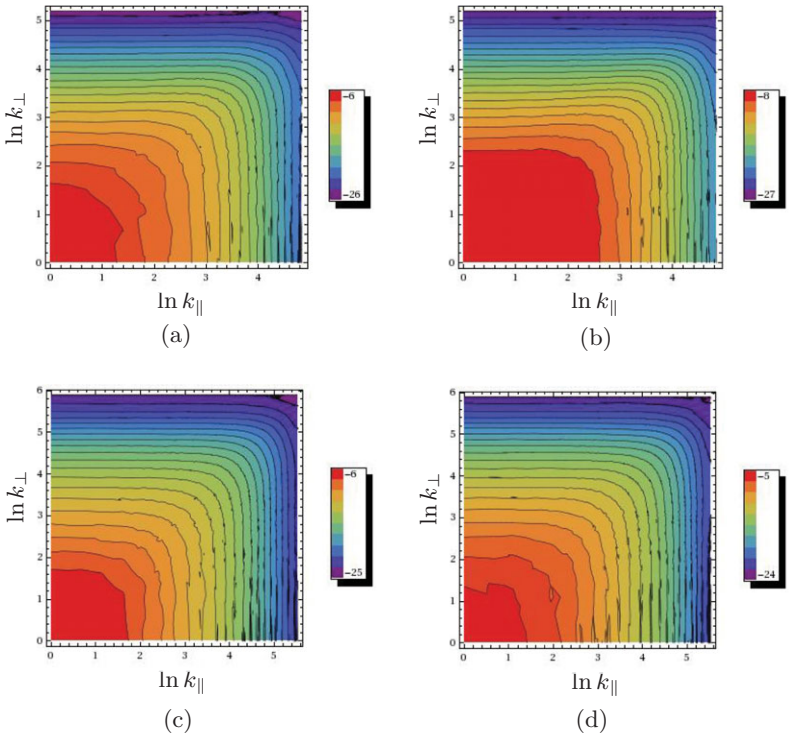


Figure 12. (Colour online) P_K in the saturated state of the turbulence simulated on a 256^3 and a 512^3 grid. $\beta = 0.01$ incompressible (a) and compressible (b) driving simulated on a 256^3 grid; $\beta = 10$ incompressible (c) and compressible (d) driving simulated on a 512^3 grid.

For $\beta = 0.01$, it can be seen that for incompressible driving, P_B has the same perpendicular preferred direction as that we find for P_K, P_{Shear} (see Fig. 11a), whereas for compressible driving there is no preferred direction (see Fig. 11b). In Fig. 9(a), it can be seen that for incompressible driving, much more incompressible modes than compressible modes are in the system. This is why we would also expect a perpendicular cascade to build up. For the case of compressible driving (see Fig. 9b), we have only slightly more incompressible than compressible modes in the system. In this case, the magnetic energy will cascade in parallel and perpendicular direction. One requirement is that magnetic and kinetic energy may cascade differently. The spectra suggest that this is indeed what happens in the simulations, but an explanation is hard.

For $\beta = 10$, the two-dimensional spectra are quite isotropic as we would predict it for this widely hydrodynamical case (see Figs. 11c, 11d, 12c, 12d, 13c, 13d, 14c and 14d).

Similar investigations have been carried out by Vestuto et al. (2003) for the case of incompressible driving in the saturated state of the spectrum. They also found a perpendicular preference of the fluctuations for small values of the plasma-β, which disappears for higher β.

5. Discussion

In this paper, we presented results from simulations of compressible MHD turbulence for low- and high-β plasmas with compressible and incompressible driving. Our special focus was on the evolution of turbulence. We found an obvious influence of the plasma-β and the type of driving on the anisotropy and the temporal energy evolution. Especially, the influence of the driver has not yet been discussed for MHD plasmas.

This may have an influence on a number of astrophysical scenarios. When assuming supernovae as energy input, it is evident that e.g. the pile-up of fluctuation energy due to the slow tangling of magnetic field lines may be observed in the early stages as a lower temperature of the plasma. Therefore, by observing temperature evolution in turbulent driving, it should be possible to determine which process is really driving the turbulence: incompressible or compressible fluctuations.

Even more striking is the influence on particle acceleration in evolving turbulence. Here also, early supernova remnants are the object of interest. The first thing to observe here is that a weak cascade in compressible driving may prevent low energetic particles to be accelerated due to missing energy at their respective resonant high wave numbers.

It is not completely clear if the anisotropy arising in the first place will have an observable effect, but it is very well possible that the anisotropy in the magnetic fluctuations may change the transport and consequently the acceleration and escape of cosmic ray from turbulent regions.

6. Summary

This paper presented a summary of the evolution of turbulence in an MHD-driven plasma. The evolution

https://doi.org/10.1017/S0022377813000147 Published online by Cambridge University Press

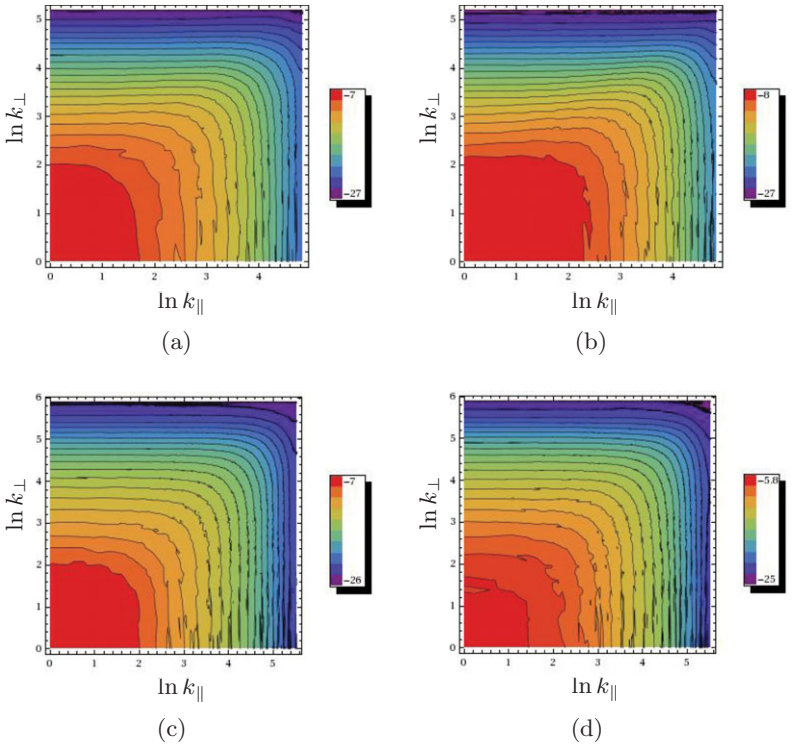


Figure 13. (Colour online) P_{Shear} in the saturated state of the turbulence simulated on a 256^3 and a 512^3 grid. $\beta = 0.01$ incompressible (a) and compressible (b) driving simulated on a 256^3 grid; $\beta = 10$ incompressible (c) and compressible (d) driving simulated on a 512^3 grid.

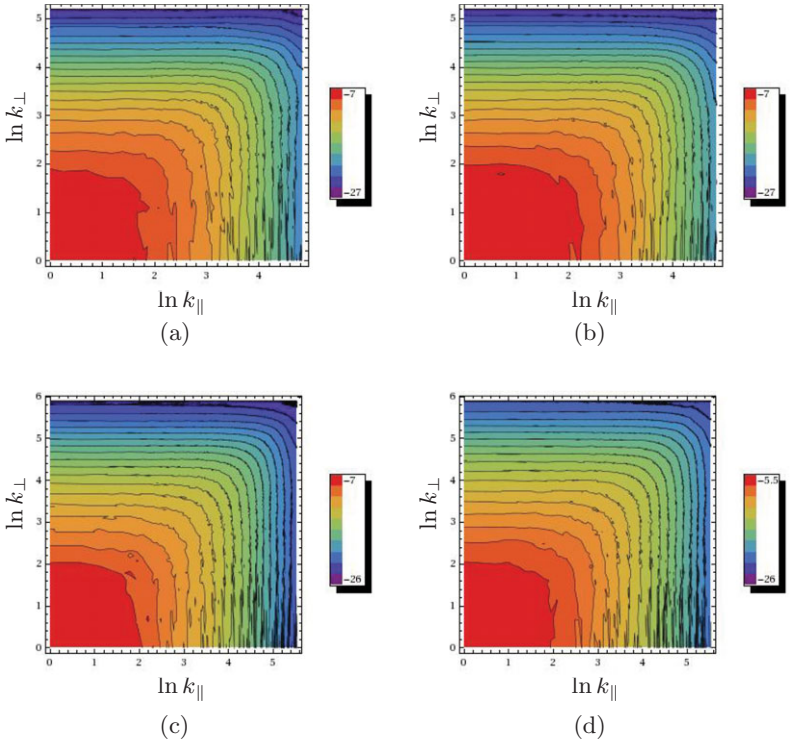


Figure 14. (Colour online) P_{Comp} in the saturated state of the turbulence simulated on a 256^3 and a 512^3 grid. $\beta = 0.01$ incompressible (a) and compressible (b) driving simulated on a 256^3 grid; $\beta = 10$ incompressible (c) and compressible (d) driving simulated on a 512^3 grid.

https://doi.org/10.1017/S0022377813000147 Published online by Cambridge University Press

is described especially under the influence of different driving mechanisms (compressible and incompressible). First principles are able to explain the spectra for the very early development of turbulence. The anisotropy of wave generation is able to explain the specific features visible. For the further development of turbulence, the plasma-β plays an essential role in the saturation of the spectra. We have shown the distribution of energy between magnetic and kinetic energy depending on the plasma-β . The results shown here are in agreement with earlier research carried out for hydrodynamics and goes into more detail regarding the specific anisotropy introduced with the background field.

Acknowledgements

MW acknowledges support by Graduiertenkolleg 1147 and FS acknowledges support by Deutsche Forschungsgemeinschaft, DFG project number Sp 1124/3. We would like to thank the anonymous referee for detailed comments that helped improving this paper.

Appendix. Measure of the anisotropy

Anistropy is one of the main features discussed in the context of this paper. The qualitative behaviour of the anisotropy can be seen in the two-dimensional plots of the spectrum. A quantitative description is far more difficult since the actual shape of the two-dimensional spectra may differ strongly.

To give a rough quantitative comparison, we try to boil down the plot to single numbers. We use the contour lines to find a $k_\perp^{\mathrm{aniso}}(k_\parallel)$. By following a contour line starting at a given value of $k_\parallel$ from the $k_\parallel$ axis to the $k_\perp$ axis, we find this parameter.

We want to illustrate the determination with a sample anisotropic function

$$f(x,y) = \frac{1}{(x^2 + \Lambda y^2)^{\frac{5}{3}12}}. \qquad \text{(A 1)}$$

The contour plots for different parameters Λ are shown in Fig. A.1. For the simple case of $\Lambda = 1$, we find for example $k_\perp^{\mathrm{aniso}}(2.3) = 2.3$. The ratio of $k_\parallel$ and $k_\perp$ is here 1, since the function is anisotropic. For $\Lambda = 0.1$, we find $k_\perp^{\mathrm{aniso}}(1.7) = 2.7$ and for $\Lambda = 10$ we find $k_\perp^{\mathrm{aniso}}(2.6) = 1.6$.

This number gives a first quantitative hint on the anisotropy of the problem, but it is limited to axis-aligned asymmetry. For a feature propagating at 45° to the magnetic field, it does not show any features.

References

Armstrong, J. W., Rickett, B. J. and Spangler, S. R. 1995 Electron density power spectrum in the local interstellar medium. *Astrophys. J.* **443**, 209–221.

Beresnyak, A. and Lazarian, A. 2009 Comparison of spectral slopes of magnetohydrodynamic and hydrodynamic turbulence and measurements of alignment effects. *Astrophys. J.* **702**, 1190–1198.

Chandran, B. D. G. 2005 Weak compressible magnetohydrodynamic turbulence in the solar corona. *Phys. Rev. Lett.* **95**(26), 265004.

Chandran, B. D. G. 2008 Weakly turbulent magnetohydrodynamic waves in compressible low-β plasmas. *Phys. Rev. Lett.* **101**(23), 235004.

Chernyshov, A. A., Karelsky, K. V. and Petrosyan, A. S. 2007 Development of large eddy simulation for modeling of decaying compressible magnetohydrodynamic turbulence. *Phys. Fluids* **19**(5), 055106.

Chernyshov, A. A., Karelsky, K. V. and Petrosyan, A. S. 2009 Validation of large eddy simulation method for study of flatness and skewness of decaying compressible magnetohydrodynamic turbulence. *Theor. Comput. Fluid Dyn.* **23**, 451–470.

Chin, Y.-C. and Wentzel, D. G. 1972 Nonlinear dissipation of Alfvén waves. *Astrophys. Space Sci.* **16**, 465–477.

Cho, J. and Lazarian, A. 2002 Compressible sub-Alfvénic MHD turbulence in low-β plasmas. *Phys. Rev. Lett.* **88**(24), 245001.

Cho, J. and Lazarian, A. 2003 Compressible magnetohydrodynamic turbulence: mode coupling, scaling relations, anisotropy, viscosity-damped regime and astrophysical implications. *Mon. Not. R. Astron. Soc.* **345**, 325–339.

Cho, J. and Vishniac, E. T. 2000 The anisotropy of magnetohydrodynamic Alfvénic turbulence. *Astrophys. J.* **539**, 273–282.

Elmegreen, B. G. and Scalo, J. 2004 Interstellar turbulence I: observations and processes. *Ann. Rev. Astron. Astrophys.* **42**, 211–273.

Federrath, C., Chabrier, G., Schober, J., Banerjee, R., Klessen, R. S. and Schleicher, D. R. G. 2011 Mach number dependence of turbulent magnetic field amplification: solenoidal versus compressive flows. *Phys. Rev. Lett.* **107**(11), 114504.

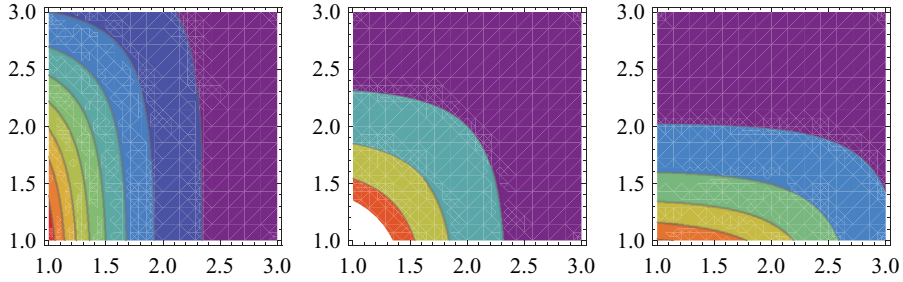


Figure A.1. (Colour online) Two-dimensional spectra for the sample spectrum (A 1). Shown are plots for the values of $\Lambda = 0.1, 1, 10$.

https://doi.org/10.1017/S0022377813000147 Published online by Cambridge University Press

Federrath, C., Klessen, R. S. and Schmidt, W. 2008 The density probability distribution in compressible isothermal turbulence: solenoidal versus compressive forcing. *Astrophys. J. Lett.* **688**, L79–L82.

Federrath, C., Roman-Duval, J., Klessen, R. S., Schmidt, W. and Mac Low, M.-M. 2010 Comparing the statistics of interstellar turbulence in simulations and observations. Solenoidal versus compressive turbulence forcing. *Astron. Astrophys.* **512**, A81.

Frisch, U. 1995 *Turbulence: The Legacy of A. N. Kolmogorov*. Cambridge: Cambridge University Press.

Goldreich, P. and Sridhar, S. 1995 Toward a theory of interstellar turbulence. 2: strong alfvenic turbulence. *Astrophys. J.* **438**, 763–775.

Grauer, R., Krug, J. and Marliani, C. 1994 Scaling of high-order structure functions in magnetohydrodynamic turbulence. *Phys. Lett.* A **195**, 335–338.

Haverkorn, M., Katgert, P. and de Bruyn, A. G. 2004 Structure in the polarized galactic synchrotron emission, in particular 'depolarization canals'. *Astron. Astrophys.* **427**, 549–559.

Klessen, R. S. 2000 One-point probability distribution functions of supersonic turbulent flows in self-gravitating media. *Astrophys. J.* **535**, 869–886.

Kolmogorov, A. 1941 The local structure of turbulence in incompressible viscous fluid for very large Reynolds' numbers. *Akademiia Nauk SSSR Doklady* **30**, 301–305.

Kowal, G., Lazarian, A. and Beresnyak, A. 2007 Density fluctuations in MHD turbulence: spectra, intermittency, and topology. *Astrophys. J.* **658**, 423–445.

Kurganov, A. and Levy, D. 2000 A third-order semi-discrete central scheme for conservation laws and convection–diffusion equations. arXiv:math/0002133. Published on ArXiv only.

Kuznetsov, E. A. 2001 Weak magnetohydrodynamic turbulence of a magnetized plasma. *Sov. J. Exp. Theor. Phys.* **93**, 1052–1064.

Lazar, M., Spanier, F. and Schlickeiser, R. 2003 Linear damping and energy dissipation of shear Alfvén waves in the interstellar medium. *Astron. Astrophys.* **410**, 415–424.

Lazarian, A. and Pogosyan, D. 1997 Interstellar filaments and the statistics of galactic HI. *Astrophys. J.* **491**, 200.

Lemaster, M. N. and Stone, J. M. 2009 Dissipation and heating in supersonic hydrodynamic and MHD turbulence. *Astrophys. J.* **691**, 1092–1108.

Lithwick, Y. and Goldreich, P. 2001 Compressible Magnetohydrodynamic Turbulence in Interstellar Plasmas. *Astrophys. J.* **562**, 279–296.

Maron, J. and Goldreich, P. 2001 Simulations of incompressible magnetohydrodynamic turbulence. *Astrophys. J.* **554**, 1175–1196.

Padoan, P., Juvela, M., Kritsuk, A. and Norman, M. L. 2006 The power spectrum of supersonic turbulence in perseus. *Astrophys. J. Lett.* **653**, L125–L128.

Politano, H. and Pouquet, A. 1995 Model of intermittency in magnetohydrodynamic turbulence. *Phys. Rev.* E **52**, 636–641.

She, Z.-S. and Leveque, E. 1994 Universal scaling laws in fully developed turbulence. *Phys. Rev. Lett.* **72**, 336–339.

Shebalin, J. V., Matthaeus, W. H. and Montgomery, D. 1983 Anisotropy in MHD turbulence due to a mean magnetic field. *J. Plasma Phys.* **29**, 525–547.

Skilling, J. 1975 Cosmic ray streaming. III - Self-consistent solutions. *Mon. Not. R. Astron. Soc.* **173**, 255–269.

Spanier, F. and Schlickeiser, R. 2005 Damping and wave energy dissipation in the interstellar medium. II. Fast magnetosonic waves. *Astron. Astrophys.* **436**, 9–16.

Sridhar, S. and Goldreich, P. 1994 Toward a theory of interstellar turbulence. 1: weak Alfvenic turbulence. *Astrophys. J.* **432**, 612–621.

Vainio, R. and Spanier, F. 2005 Evolution of Alfvén waves by three-wave interactions in super-Alfvénic shocks. *Astron. Astrophys.* **437**, 1–8.

Vestuto, J. G., Ostriker, E. C. and Stone, J. M. 2003 Spectral properties of compressible magnetohydrodynamic turbulence from numerical simulations. *Astrophys. J.* **590**, 858–873.

von Weizsäcker, C. F. 1951 The evolution of galaxies and stars. *Astrophys. J.* **114**, 165.

https://doi.org/10.1017/S0022377813000147 Published online by Cambridge University Press